Publisher: GSA
Journal: GEOL: Geology
DOI:10.1130/G39045.1

Magmatic-tectonic conditions for hydrothermal venting on an ultraslow-spread oceanic core complex

Jennifer L. Harding[1], Harm J.A. Van Avendonk[1], Nicholas W. Hayman[1], Ingo Grevemeyer[2], Christine Peirce[3], and Anke Dannowski[2]

[1]Institute for Geophysics, Jackson School of Geosciences, University of Texas at Austin, J.J. Pickle Research Campus, 10100 Burnet Road, Building 196, Austin, Texas 78758, USA

[2]GEOMAR Helmholtz Centre of Ocean Research, Wischhofstr. 1-3, D-24148 Kiel, Germany

[3]Department of Earth Sciences, University of Durham, South Road, Durham DH1 3LE, UK

ABSTRACT

Hydrothermal venting, an important cooling mechanism of the Earth, supports a diverse array of seafloor and sub-seafloor ecosystems that are sustained by large thermal and chemical fluxes. Vents have been found along even the slowest and coldest spreading centers, calling into question the driving heat source for these vents. The ultraslow-spreading Mid-Cayman Spreading Center in the Caribbean Sea, which hosts the axial-flank Von Damm Vent Field (VDVF), provides an opportunity to probe the mechanisms for venting at ultraslow spreading rates. Using active-source seismic data from the 2015 CaySeis experiment, we determined the seismic velocities in the large massif beneath the VDVF. We propose that this massif was produced by a pulse of on-axis magmatism ~2 Mya, which was then followed by exhumation, cooling, and fracturing. A low seismic

velocity anomaly 5 km below the VDVF is evidence for either a cracking front mining lithospheric heat or intrusive magmatic sills, both of which could drive ongoing deep hydrothermal fluid circulation. We conclude that the transient magmatism and variable crustal thickness at ultraslow-spreading centers create conditions for long-lived hydrothermal venting that may be widespread, and other VDVF-like vents may be common in these areas.

INTRODUCTION

Mid-ocean ridge hydrothermal vents display a wide range of thermal and chemical properties that support diverse, extremophile communities (e.g., Kelley et al., 2002). The most numerous mid-ocean ridge vents occur along faster-spreading, hotter ridges, which spread at full-rates of > 75 mm yr^{-1} from axes with depths shallower than 4000 mbsl (meters below sea-level) and accrete oceanic crust of a relatively uniform, symmetrically-spread 6–7 km thickness (White et al., 2001). This uniform crustal thickness is a result of efficient mantle melting and consistent melt extraction, geochemically expressed by dilute incompatible element concentrations (Gale et al., 2014). Hydrothermal vents, however, also exist on colder, slower-spreading centers with lower mantle potential temperatures and thus lower extents of melting (Dalton et al., 2014) and decreased, sporadic volcanism (Dick et al., 2003; Rubin and Sinton, 2007), which produces heterogeneous crust (Fig. DR1). This crustal heterogeneity is most pronounced along ridges that spread at ultraslow rates <20 mm yr^{-1} (Dick et al., 2003) with axial depths that are generally > 4000 mbsl (Dick et al., 2003). Though hydrothermal vents on ultraslow-spreading centers have been found (e.g., Michael et al., 2003), their abundance, distribution, and nature is relatively unknown.

Several vent fields along slow- (20–60 mm yr^{-1}) spreading centers, notably the Lost City Field (e.g., Früh-Green et al., 2003) and the Rainbow Vent (e.g. Canales et al., 2017) on the Mid-Atlantic Ridge have also been discovered in off-axis regions and/or where volcanism is sparse. Though the role of magmatism in driving some types of hydrothermal venting at these settings is uncertain, the amount of magmatism clearly influences the seafloor morphology of off-axis vent localities, which can be either symmetric or asymmetric about the central axis. Slow and ultraslow seafloor spreading can switch between symmetric and asymmetric modes on a ~1–2 My timescale (Tucholke et al., 2008), with the transitions caused by the change in ratio of magmatism relative to tectonism (Buck et al., 2005). Symmetric seafloor develops when this ratio is either very low or high. If magmatism is high, then the seafloor is characterized by high-angle normal faults dipping toward the axis. In cases of extremely little magmatism, which is common on ultraslow-spreading segments, the "smooth" seafloor develops as predominantly mantle peridotite is exhumed (Cannat et al., 2003). When this magmatic-tectonic ratio is low-to-moderate (~0.3-0.5), however, asymmetric ridge segments tend to form as long-lived detachment faults exhume lower-crustal and/or upper-mantle rock, forming oceanic core complexes (OCCs) (Olive et al., 2010).

Previous models have proposed that the death of an OCC is marked by an episode of magmatism and generation of OCC-cutting high-angle faults (MacLeod et al., 2009). This "life-cycle" of OCCs in turn affects the type of hydrothermal activity (McCaig et al., 2007), though it is unclear if such venting is driven by deep magmatism (Allen and Seyfried, 2004), serpentinization (Früh-Green et al., 2003) and/or lithospheric heat that is channeled by deeply penetrating faults (Lowell et al., 2017). Moreover, if magmatism is fluctuating around a lower average at ultraslow-spreading centers than at slow-spreading centers (Rubin and Sinton, 2007), then the life cycle of OCCs at more magma-poor ultraslow-spreading centers may differ from this model, where an increase in magmatism causes an OCC-mode of seafloor spreading, and a decrease in magmatism marks the death of the detachment fault. The Mid-Cayman Spreading Center (MCSC) plays a special role in this discussion because it has been long-thought to be an and is an end-member in axial depth, crustal thickness, and cold mantle potential temperature (Hayman et al., 2011; Klein and Langmuir, 1987; ten Brink et al., 2002), yet it hosts at least two hydrothermal vents, one of which sits on the summit of a large OCC (German et al., 2010; Connelly et al., 2012). Here, we use recently acquired seismic data to help constrain the development of the OCC and its hydrothermal vent, and evaluate the role of magmatism in this process.

THE MID-CAYMAN SPREADING CENTER AND THE VON DAMM VENT FIELD

The ~110 km-long MCSC is located between transform fault zones that separate the Caribbean from the North American plate (Fig. 1), and accommodating a local discrepancy in plate motion results in one of the slowest orthogonal rates (~15 mm yr^{-1}) globally. In the central portion of the MCSC, an OCC named “Mt. Dent” (Edgar et al., 1991) rises ~3 km from the adjacent axial rift, and the Von Damm Vent Field (VDVF) was discovered near its summit in 2010 (Connelly et al., 2012). The Mt. Dent OCC is quite mature in the sense of MacLeod et al. (2009), as shown by both the age range across the OCC (likely 1.5-2 My) (Fig. DR10), and steep faults that cut the detachment surface (Stroup and Fox, 1981). Additionally, a linear feature, potentially an axial-volcanic ridge (AVR), cuts obliquely across the deep southern rift of the MCSC, trending north-northwest directly into Mt. Dent. It has not been established whether this feature has caused recent volcanism near or on Mt. Dent, though pillow basalts of unknown provenance have been reported (Stroup and Fox, 1981; Van Dover et al., 2014). If so, the AVR could signify the propagation of magmatism into the "dying" OCC (MacLeod et al., 2009).

Ultramafic and mafic gabbroic rocks have been sampled around the VDVF and along the adjacent detachment fault surface (Hayman et al., 2011; Stroup and Fox, 1981) suggesting the OCC was magmatically constructed, but serpentinized peridotites have also been sampled both near the termination of the detachment as well as areas to the south (Fig. 1). Similarly, the ~200 °C, moderate-pH vent fluids have geochemical compositions consistent with very long residence times in fractured crustal rocks (McDermott et al., 2015), yet the high Mg concentrations, including the local precipitation of talc, suggests a partly ultramafic, possibly mantle host (Hodgkinson et al., 2015). Moreover, while emitting only moderate-temperature fluids, the heat flux is similar to high-temperature vents associated with magmatism, but low H_2S concentrations suggest nominal magmatic input (Hodgkinson et al., 2015). It therefore remains unclear whether Mt. Dent is primarily a crustal or mantle dominated OCC and to what extent magmatism is involved in driving the VDVF.

CAYSEIS SEISMIC PROFILE ACROSS MT. DENT

In order to determine the crustal and upper mantle structure beneath the VDVF, we conducted the Cayman Seismic (CaySeis) experiment during April, 2015 aboard the *F/S Meteor* (Cruise M115), a multi-national collaboration to collect wide-angle, ocean-bottom seismic refraction and under way geophysical data of the MCSC. Through tomographic inversion of P-wave first arrival times from the wide-angle refraction data (Van Avendonk et al., 1998; Van Avendonk et al., 2001) (Supp. Methods), we produced a 2D P-wave seismic velocity (Vp) profile along Line 2, which crosses the neovolcanic zone, Mt. Dent, and the VDVF (Fig. 1). In the tomographic image (Fig. 2), the velocity structure to the east and west of Mt. Dent is fairly homogenous with a steady change in Vp from ~3.5–4.0 km s^{-1} near the seafloor to ~7.5–8.0 km s^{-1} at depths of ~3–4 km below the seafloor. In contrast, in the vicinity of Mt. Dent and the VDVF, near-surface Vp reaches 6.0 km s^{-1}. Mt. Dent exhibits a 10–15 km by ~3 km body with a Vp of nearly 6.5 km s^{-1} that dips ~20° upwards toward the west. Beneath this zone of high Vp at 4.0–7.0 km below Mt. Dent, Vp is as low as ~6.0 km s^{-1}. At larger depth, Vp increases gradually to 7.5 km s^{-1} at ~9.5 km below the seafloor.

In our view, the high Vp (6.5 km s^{-1}) at shallow depth beneath Mt. Dent is best explained by a gabbro body, or a dense cluster of gabbro bodies, that has not been extensively altered and does not have many open fractures, based on observations in similar settings (Canales et al., 2008). This high-Vp body is not likely composed of much mantle peridotite because serpentinization near the surface would likely result in a Vp well below the observed 6.0 km s^{-1}, nor can Mt. Dent host a thick basaltic section because high-porosity basalt has a Vp < 6.0 km s^{-1} (Christensen, 1996). In contrast, the 6.0 km s^{-1} Vp at larger depths beneath the summit of Mt. Dent could be caused by either fluid-filled fractures, high temperatures, or partial melt in either crustal or mantle rock, because the Vp of gabbro and peridotite would otherwise be on the order of > 6.0 km s^{-1} according to widely used empirical relationships (Christensen, 1996). The gravity anomaly associated with Mt. Dent is consistent with this interpretation as well, with the free air anomaly fit well by a large low-density region (Fig. DR10). We return to the alternative interpretations of this deeper zone of relatively low Vp in the following Discussion.

Immediately adjacent to Mt. Dent, on axis, there is no seismic evidence for a thick (> ~1 km) layer of young igneous crust, as the Vp of the shallow lithosphere is ~3.5–4.0 km s^{-1}, high for young extrusive basalts, increasing with depth with a constant gradient to a mantle Vp of 7.5–8.0 km s^{-1} at ~5.0 km beneath the axis. The velocity gradient further suggests that on-axis to the east of Mt. Dent there is currently little magmatism and low temperatures persist. The velocity structure of the shallow basement to the west of Mt. Dent and east of the MCSC is consistent with either thin volcanic crust and/or serpentinized mantle, but due to the ambiguity of relating Vp to lithology, distinguishing basalt from serpentinite requires alternative data sets. At depths of ~3.5–4.0 km below the seafloor, Vp reaches 8.0 km s^{-1}, indicating unaltered mantle.

DISCUSSION

Given the new seismic velocity image of the axial valley and Mt. Dent (Fig. 2) and the notion that the MCSC is subject, overall, to low extents of melting, we present two alternative models for the formation and evolution of Mt. Dent (Fig. 3). Both invoke the rolling hinge model (e.g., Lavier et al., 1999) wherein the inclined gabbro body, or bodies, and overall lack of volcanic cover on Mt. Dent arises from flexural rotation of the once steep detachment fault to shallow angles as the OCC was exhumed from beneath the brittle-ductile transition (e.g. Hayman et al., 2011). Initially, magmatism in this central portion of the MCSC was low and symmetric seafloor spreading produced either thin crust or smooth, mantle-dominated seafloor. An increase in magmatism ~2 Mya along this portion of the spreading center produced the gabbroic intrusion deep beneath the axial valley (Fig. 3A), initiating an asymmetric period of seafloor spreading. During this magmatic pulse, an eastwardly-dipping detachment fault began to exhume and rotate the plutonic body from beneath the axial valley. Exhumation likely occurred most rapidly ~1 Mya, prior to the development of the central anomaly magnetic high on the eastern flank of Mt. Dent (Fig. DR10). Basaltic crust that formed during this magmatic, asymmetric phase was stripped from the OCC and is now preserved on the eastern flank of the MCSC. Magmatism on axis has since waned and the gabbroic intrusion in Mt. Dent has cooled.

We propose two alternate models to explain the seismic velocity structure and the presence of the VDVF. In the first model (Fig 3B), the region of low Vp is interpreted as a cracking front. During exhumation, Mt. Dent underwent faulting and fracturing in response to flexure and uplift relative to the rift axis and faults and fractures propagated through Mt. Dent. Once slip on the detachment fault ceased, continued tectonic extension throughout Mt. Dent caused deep cracking, allowing for hydrothermal circulation and initiating the VDVF. The cracking front under Mt. Dent defines an area at the base of the lower crustal, now cooled, plutonic body. There, cracks can be transiently open so as to feed the vent and cause the low-Vp zone, while fractures are mostly sealed in the high-Vp gabbro body. Such transient opening and closing of cracks due to evolving thermomechanical conditions is a central premise of many structurally controlled hydrothermal systems (e.g., Sibson, 1990) and recent analytical modeling finds that deep crustal faulting can drive moderate-temperature venting without magmatic input (Lowell et al., 2017). If true, the heat of exhumation, along with heat from serpentinization

DOI:10.1130/G39045.1

reactions of the peridotite in Mt. Dent, may be enough to fuel the VDVF. The "cracking front" model is supported by the long hydrothermal fluid residence times and low magmatic heat input required by the geochemistry of the vent fluids (Hodgkinson et al., 2015).

The second model (Fig. 3B) interprets the low-Vp zone as elevated temperature or partial melt, caused by off-axis magmatic intrusion into the deeper, ultramafic part of Mt. Dent. This model would satisfy the argument that a magmatic heat source is necessary for driving venting (Baker, 2009). The possible north-northwest trending AVR (Fig. 1) intersects Mt. Dent near the VDVF, and a small episode of magmatism could intrude magmatic sills into the base of the already-permeable Mt. Dent where Vp appears depressed, driving the VDVF and causing local basaltic eruptions. We suggest, however, that it is unlikely there is active magmatism and diking within Mt. Dent today, because such magmatism would cause Vp deep in Mt. Dent to be lower and sampled by less rays. Alternatively, there could be out-of-plane magmatism that could not be imaged by the 2-D seismic line, leading to partially-molten sills in the OCC, as has been suggested for the Rainbow vent on the MAR (Canales et al., 2017).

Ultraslow spreading centers are, in general, in remote parts of the globe, and thus acquiring data to predict the conditions that favor VDVF-type vents *a priori* is highly desirable. We argue that the fluctuation of magmatism that is typical of ultraslow-spreading centers produces variable crustal thickness and plays a role in the life cycle of the Mt. Dent OCC and its hydrothermal vent. Whether magmatism is needed to drive the VDVF, however, is still in question. If the cracking front model is correct, then the death of Mt. Dent was not marked by magmatism, but instead by a decrease in magmatism, as

DOI:10.1130/G39045.1

might be predicted in a colder, less magmatic setting. If this sill intrusion model is correct, however, then the death of Mt. Dent may have been caused by an episode of magmatism within the OCC, and this may be a common feature among all OCCs. Further modeling of how lithospheric heat could drive moderate temperature vents, or other data sets in the MCSC, like seismic reflection data or higher resolution geophysical research, could help elucidate this outstanding problem. If VDVF-type vents are common at ultraslow-spreading centers, they would broaden the types of microbial, biological, and chemical exchanges that occur in these environments.

ACKNOWLEDGMENTS

We thank the captain and crew of the *F/S Meteor,* the technicians of the NERC's Ocean-Bottom Instrumentation Facility (OBIF (Minshull et al., 2005)), GEOMAR, UTIG, and NEPA, including Steffen Saustrup, Anatoly Mironov, Cord Papenberg, Mahshid Erfanian Mehr, Andrew Clegg, and Ben Pitcairn; We also thank NSF (OCE-1356895), DFG, and NERC (NE/K011162/1) for funding this project. This is UTIG contribution xxxx.

REFERENCES CITED

Allen, D.E., and Seyfried, W.E., 2004, Serpentinization and heat generation: constraints from Lost City and Rainbow hydrothermal systems: Geochimica et Cosmochimica Acta, v. 68, no. 6, p. 1347-1354. doi:10.1016/j.gca.2003.09.003.

Baker, E.T., 2009, Relationships between hydrothermal activity and axial magma chamber distribution, depth, and melt content: Geochemistry, Geophysics, Geosystems, v.10, no.6, doi:10.1029/2009gc002424

Buck, R.W., Lavier, L.L., and Poliakov, A.N.B., 2005, Modes of faulting at mid-ocean ridges: Nature, v. 434, p. 719–723, doi:10.1038/nature03358.

Canales, J.P., Tucholke, B.E., Xu, M., Collins, J.A., and DuBois, D.L., 2008, Seismic evidence for large-scale compositional heterogeneity of oceanic core complexes: Geochemistry Geophysics Geosystems, v. 9, Q08002, doi:10.1029/2008GC002009.

Canales, J.P., Dunn, R.A., Arai, R., and Sohn, R. A., 2017, Seismic imaging of magma sills beneath an ultramafic-hosted hydrothermal system: Geology. v. 25, no. 5, p. 451-454, doi:10.1130/G38795.1.

Cannat, M., Rommevaux-Jestin, C., and Fujimoto, H., 2003, Melt supply variations to a magma-poor ultra-slow spreading ridge (Southwest Indian Ridge 61° to 69°E): Geochemistry Geophysics Geosystems, v. 4, p. 9104, doi:10.1029/2002GC000480.

Christensen, N.I., 1996, Poisson’s ratio and crustal seismology: Journal of Geophysical Research. Solid Earth, v. 101, p. 3139–3156, doi:10.1029/95JB03446.

Connelly, D.P., et al., 2012, Hydrothermal vent fields and chemosynthetic biota on the world’s deepest seafloor spreading centre: Nature Communications, v. 3, p. 620, doi:10.1038/ncomms1636.

Dalton, C.A., Langmuir, C.H., and Gale, A., 2014, Geophysical and Geochemical Evidence for Deep Temperature Variations Beneath Mid-Ocean Ridges: Science, v. 344, p. 80–83, doi:10.1126/science.1249466.

Dick, H.J.B., Lin, J., and Schouten, H., 2003, An ultraslow-spreading class of oceanic ridge: Nature, v. 426, p. 405–412, doi:10.1038/nature02128.

Edgar, T. N., Dillon, W. P., Parson, L. M., Scanlon, K. M., Jacobs, C. L., and Holcombe, T., L., 1991, GLORIA sidescan-sonar image and interpretation of the central

Cayman trough, northwestern Caribbean Sea, U.S. Geological Survey Miscellaneous Field Investigations Map MF 2083-A: Reston, Virginia, United States Geological Survey.

Früh-Green, G.L., Kelley, D.S., Bernasconi, S.M., Karson, J.A., Ludwig, K.A., Butterfield, D.A., Boschi, C., and Proskurowski, G., 2003, 30,000 Years of Hydrothermal Activity at the Lost City Vent Field: Science, v. 301, p. 495–498, doi:10.1126/science.1085582.

Gale, A., Langmuir, C.H., and Dalton, C.A., 2014, The Global Systematics of Ocean Ridge Basalts and their Origin: Journal of Petrology, v. 55, p. 1051–1082, doi:10.1093/petrology/egu017.

German, C.R., Bowen, A., Coleman, M.L., Honig, D.L., Huber, J.A., Jakuba, M.V., Kinsey, J.C., Kurza, M.D., Leroy, S., McDermott, J.M., Mercier de Lepinay, B., Nakamura, K., Seewald, J.S., Smith, J.L., Sylva, S.P., Van Dover, C.L., Whitcomb, L.L., and Yoerger, D.R., 2010, Diverse styles of submarine venting on the ultraslow spreading Mid-Cayman Rise: Proceedings of the National Academy of Science, v. 107, no. 14, p. 14,020-14,025. doi:10.1073/pnas.1009205107.

Hayman, N. W., Grindlay, N. R., Perfit, M. R., Mann, P., Leroy, S., and de Lépinay, B. M., 2011, Oceanic core complex development at the ultraslow spreading Mid-Cayman Spreading Center: Geochemistry, Geophysics, Geosystems, v. 12, Q0AG02, doi:10.1029/2010GC003240.

Hodgkinson, M.R., Webber, A.P., Roberts, S., Mills, R.A., Connelly, D.P., and Murton, B.J., 2015, Talc-dominated seafloor deposits reveal a new class of hydrothermal system: Nature Communications, v. 6, p. 10150, doi:10.1038/ncomms10150.

Kelley, D.S., Baroos, J.A., and Delaney, J.R., 2002, Volcanoes, Fluids, and life at mid-ocean ridge spreading centers: Annual Review of Earth and Planetary Sciences, v. 30, no. 1, p.385-491. doi:10.1146/annurev.earth.30.091201.141331.

Klein, E.M., and Langmuir, C.H., 1987, Global correlations of ocean ridge basalt chemistry with axial depth and crustal thickness: Journal of Geophysical Research, v. 92, p. 8089–8115, doi:10.1029/JB092iB08p08089.

Lavier, L., Buck, R.W., and Poliakov, A.N.B., 1999, Self-consistent rolling-hinge model for the evolution of large-offset low-angle normal faults: Geology, v. 27, p. 1127–1130, doi:10.1130/0091-7613(1999)027<1127:SCRHMF>2.3.CO;2.

Lowell, R.P., 2017, A fault-driven circulation model for the Lost City Hydrothermal Field: Geophysical Research Letters. v. 44, doi:10.1002/2016GL072326.

MacLeod, C.J., Searle, R.C., Murton, B.J., Casey, J.F., Mallows, C., Unsworth, S.C., Achenbach, K.L., and Harris, M., 2009, Life cycle of oceanic core complexes: Earth and Planetary Science Letters, v. 287, p. 333–344, doi:10.1016/j.epsl.2009.08.016.

McCaig, A.M., Cliff, R.A., Escartin, J., Fallick, A.E., and MacLeod, C.J., 2007, Oceanic detachment faults focus very large volumes of black smoker fluids: Geology, v. 35, no. 10, p. 935-938. doi:10.1130/g23657a.1.

McDermott, J.M., Seewald, J.S., German, C.R., and Sylva, S.P., 2015, Pathways for abiotic organic synthesis at submarine hydrothermal fields: Proceedings of the National Academy of Sciences of the United States of America, v. 112, p. 7668–7672, doi:10.1073/pnas.1506295112.

Michael, P.J., Langmuir, C.H., Dick, H.J., Snow, J.E., Goldstein, S.L., Graham, D.W., Lehnert, K., Kurras, G.J., Jokat, W., Muhe, R., Edmonds, H.N., 2003, Magmatic and amagmatic seafloor generation at the ultraslow-spreading Gakkel ridge, Arctic Ocean: Nature, v. 423, p. 956-961. doi:10.1038/nature01704.

Olive, J.-A., Behn, M.D., and Tucholke, B.E., 2010, The structure of oceanic core complexes controlled by the depth distribution of magma emplacement: Nature Geoscience, v. 3, p. 491–495, doi:10.1038/ngeo888.

Rubin, K.H., and Sinton, J.M., 2007, Inferences on mid-ocean ridge thermal and magmatic structure from MORB compositions: Earth and Planetary Science Letters, v. 260, p. 257–276, doi:10.1016/j.epsl.2007.05.035.

Sibson, R.H., 1990, Conditions for fault-value behaviour. Geological Society, London, Special Puplications, v. 54, no. 1, p. 15-28. doi:10.1144/GSL.SP1990.054.01.02.

Stroup, J.B., and Fox, P.J., 1981, Geologic investigations in the Cayman Trough: Evidence for thin crust along the Mid-Cayman Rise: The Journal of Geology, v. 89, p. 395–420, doi:10.1086/628605.

ten Brink, U.S., Coleman, D.F., and Dillon, W.P., 2002, The nature of the crust under the Cayman Trough from gravity: Marine and Petroleum Geology, v. 19, p. 971-987.

Tucholke, B.E., Behn, M.D., Buck, W.R., and Lin, J., 2008, Role of melt supply in oceanic detachment faulting and formation of megamullions: Geology, v. 36, p. 455–458, doi:10.1130/G24639A.1.

Van Avendonk, H.J.A., Harding, A.J., Orcutt, J.A., and McClain, J.S., 1998, A two-dimensional tomographic study of the Clipperton transform fault: Journal of Geophysical Research, v. 103, p. 17,885–17,899, doi:10.1029/98JB00904.

Van Avendonk, H.J.A., Harding, A.J., Orcutt, J.A., and McClain, J.S., 2001, Contrast in crustal structure across the Clipperton transform fault from travel time tomography:

Journal of Geophysical Research, v. 106, p. 10,961–10,981, doi:10.1029/2000JB900459.

Van Dover, C., Marsh, L., German C., John, B., Cheadle, M., Vacchione, M., Amon, D., Ball, B., Copley, J., Smary, C., Fuller, S.A., Phillips, B.T., Cantner, K., Auscavitch, S., and Ballard, R.D., 2014, Exploration of the Mid-Cayman Rise, Oceanography, v. 27, p. 32-33.

White, R.S., Minshull, T.A., Bickle, M.J., and Robinson, C.J., 2001, Melt generation at very slow-spreading oceanic ridges: Constraints from geochemical and geophysical data: Journal of Petrology, v. 42, p. 1171–1196, doi:10.1093/petrology/42.6.1171.

FIGURE CAPTIONS

Figure 1. (A) Map and plate motions of the central Caribbean. (B) Bathymetric map of the Mid Cayman Spreading Center area of interest. White line is seismic profile Line 2, white circles are active-source ocean-bottom seismometer (OBS) stations, and the yellow star is the Von Damm Vent Field (VDVF). Green dots are dredged peridotite samples, and the red dashed lines encircle the areas that basaltic lavas have been dredged. Pie chart reflects relative abundance of lavas, gabbro, and (variably serpentinized) peridotite in dredges and dive samples from Mt. Dent (Hayman et al., 2011) (see key). The black dashed line traces the Mt. Dent detachment fault. (C) Oblique view of Mt. Dent and the possible axial volcanic ridge (AVR). The VDVF is marked by the yellow star.

Publisher: GSA
Journal: GEOL: Geology
DOI:10.1130/G39045.1

Jennifer L. Harding, Figure 1, Manuscript G39045

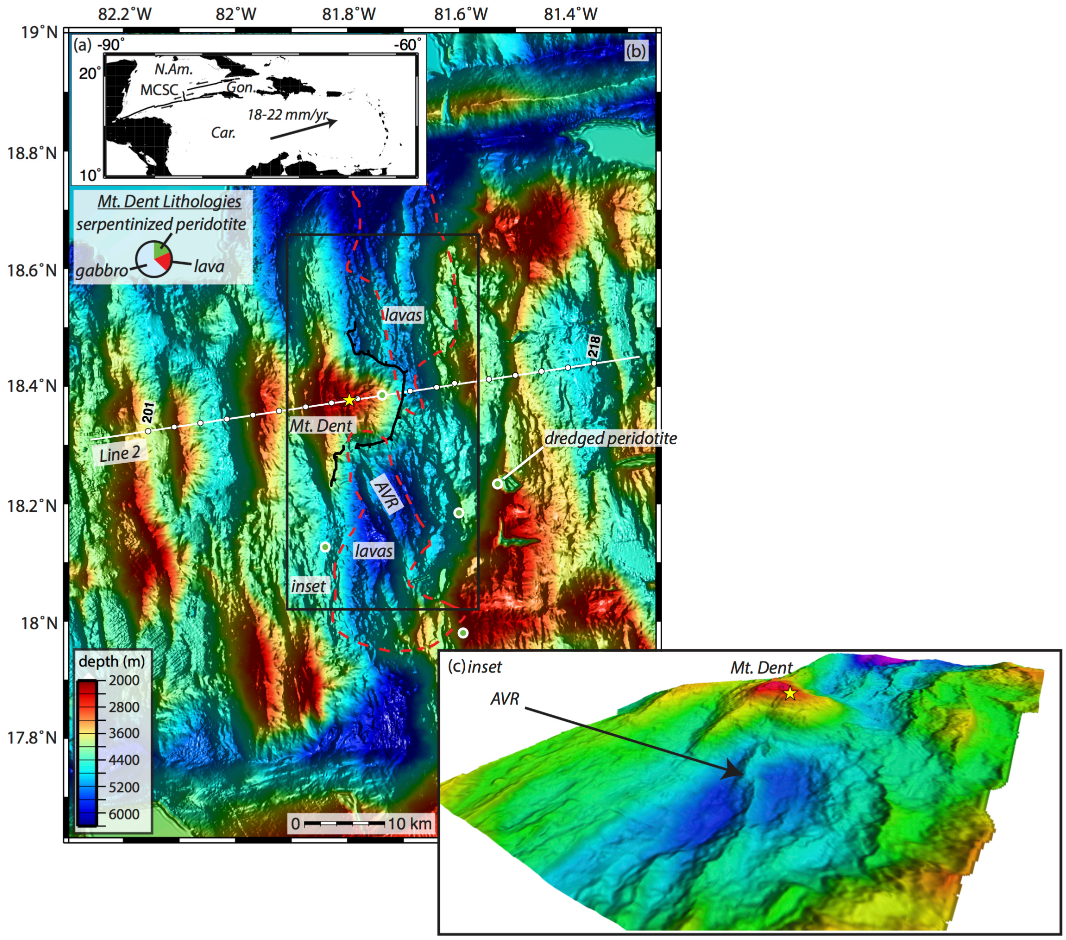

345

DOI:10.1130/G39045.1

Figure 2. Compressional seismic velocity model of Line 2 derived from wide-angle refraction data collected during the CaySeis experiment, at 2x vertical exaggeration. Solid lines are velocity contours of 1 km s^{-1} with dashed lines every 0.5 km s^{-1}. The yellow star denotes the location of the Von Damm Vent Field (VDVF). Approximate seafloor ages from identified magnetic lineations are labeled. Red and blue dashed lines correspond to 1-D profiles in Fig. DR5.

Jennifer L. Harding, Figure 2, Manuscript G39045

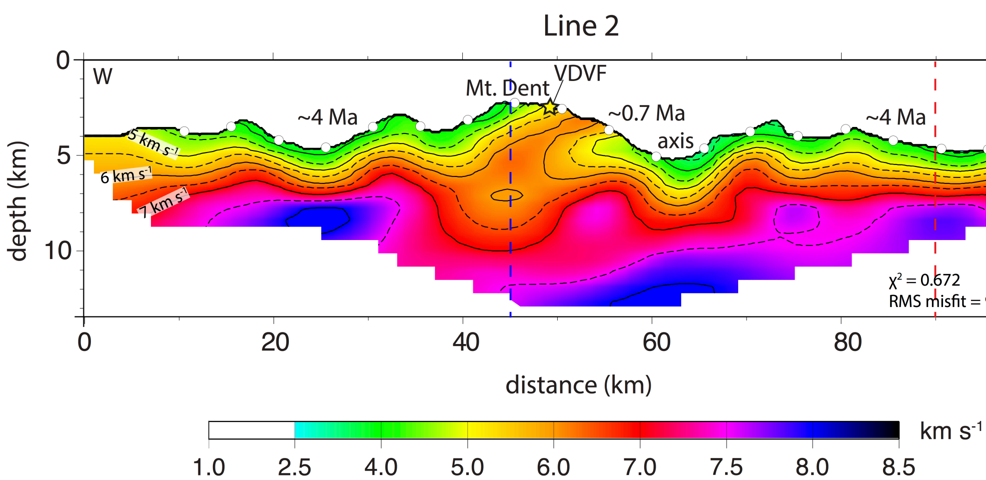

DOI:10.1130/G39045.1

Figure 3. Evolution of Mt. Dent. (A) Axial region of the Mid-Cayman Spreading Center (MCSC) along Line 2 at ~2 Mya. A gabbro (dark gray) body was produced on axis and the detachment fault began slipping. Basaltic cover (light gray) to the east fluctuates with seafloor spreading mode. Mantle peridotite (dark green) is increasingly serpentinized (light green) with shallower depths. (B) Present-day axial region of the MCSC along Line 2. The gabbro body has been exhumed and rotated in the footwall of the detachment fault, which has formed the oceanic core complex (OCC) Mt. Dent. Mt. Dent has been fractured and faulted (black lines) as magmatism decreased and extensional stress on the OCC increased, allowing for deep hydrothermal fluid circulation (possible path in blue arrows). The heat source driving venting is either magmatic sill intrusions, or lithospheric heat (light red).

Publisher: GSA
Journal: GEOL: Geology
DOI:10.1130/G39045.1

368

Jennifer L. Harding, Figure 3, Manuscript G39045

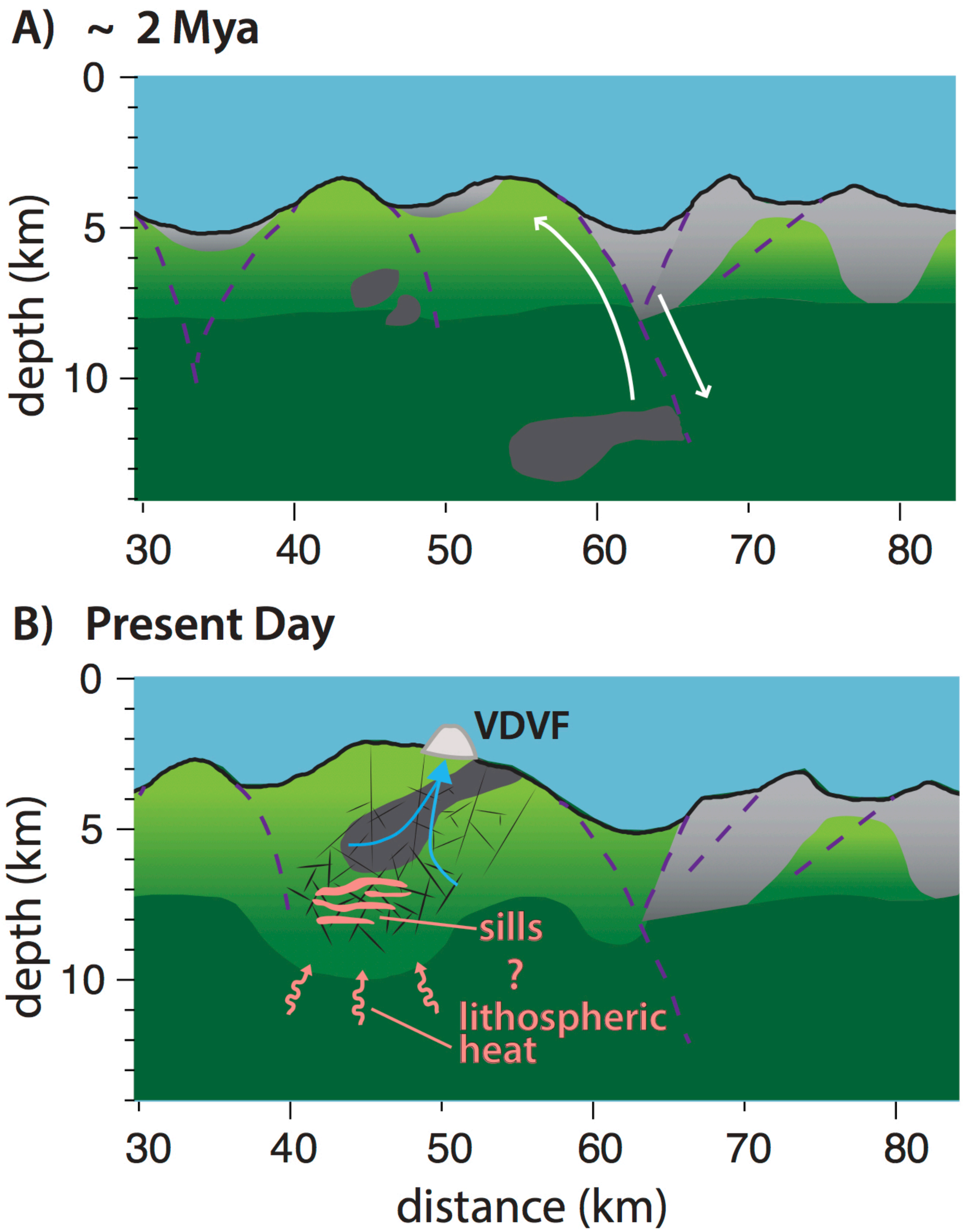

369

[1]GSA Data Repository item 2017G39045, including a description of methods, Supplementary Figures DR1-DR10, Table DR1, caption for database DR1 as well as Database DR1, and an Excel file (Moho_compilation.zip) containing oceanic crustal thickness data, is available online at http://www.geosociety.org/datarepository/2017/ or on request from editing@geosociety.org.

Publisher: GSA
Journal: GEOL: Geology
DOI:10.1130/G39045.1

Supplementary Materials for:

Magmatic-tectonic conditions for hydrothermal venting on an ultraslow-spread oceanic core complex

J.L. Harding[1*], H.J.A. Van Avendonk[1], N.W. Hayman[1], I. Grevemeyer[2], C. Peirce[3], A. Dannowski[2]

correspondence to: jharding@utexas.edu

This PDF file includes:

Methods

Figs DR1 to DR10

Table DR1

Methods

Na8.0 Compilation

The concentrations of incompatible element Na were compiled from basalts at different spreading segments around the globe with different spreading rates (*2*). Na8.0 values are normalized to a MgO wt % of 8.0 using liquid-line of descent models (*2*). Na8.0 values from locations close to hot spot influence, in particular the Afar, Iceland and Samoa hotspots. These values are plotted vs. segment spreading rate as a red cloud (Fig. DR1), as well as data points with error bars are plotted (Fig DR2).

Oceanic Crustal Thickness Compilation

Oceanic crustal thicknesses determined from over 200 seismic refraction studies were compiled with spreading rate and seafloor age extracted for each data point using isochrones (Müller et al., 2008) (see Database DR1). Data points were excluded from the compilation if they were influenced by hot spots or fracture zones. Crustal thickness vs. spreading rate is plotted as a blue cloud (Fig. DR1) and as data points with error bars (Fig. DR3), excluding data collected before 1970 and from seafloor older than 20 Ma.

Seismic Tomography

We used active-source ocean-bottom seismometer (OBS) data collected along Line 2 (Fig. 1) during the CaySeis cruise to produce the P-wave seismic velocity image (Fig. 2). An airgun array of 12 G-guns with a total volume of 84 liters was towed behind the *F/S Meteor*, producing seismic energy that was recorded by OBSs on the seafloor between 4 to 20 Hz. These OBSs were pooled from three institutions, the University of

Texas Institute for Geophysics in Austin, Texas, the NERC's Ocean-Bottom Instrumentation Facility in the UK, and the GEOMAR Centre for Ocean Research in Kiel, Germany. OBSs were spaced ~ 5 km apart along the seafloor, with shots every minute (~ 150 m shot spacing). A total of 18 OBSs comprise Line 2.

P-wave first arrival times were first picked from the wide-angle refraction data collected by each OBS (Fig. DR4). Phases were not distinguished due to the rough bathymetry and complicated structure of the Mid-Cayman Spreading Center (MCSC). These picked times were assigned an error from 50 to 200 ms based on signal to noise ratio and offset. These times were then inverted for P-wave velocities throughout a 106 x 25 km model space (Van Avendonk at al., 1998; Van Avendonk et al., 2001). Additionally, multiple refractions were picked and incorporated into the inversion in order to improve imaging of distal areas of the model space. These multiples represent P-wave refractions with an additional bounce in the water column above the OBS.

The tomographic inversion process begins with a starting seismic velocity model based on assumptions of oceanic crustal velocity structure (Fig. DR5). The raypaths from all source-receiver pairs were calculated through the starting model using a hybrid shortest path and raybending method (Van Avendonk et al., 2001) in a 3D (extended ±1.6 km perpendicular to Line 2) model space to account for the rough bathymetry. The difference between the picked P-wave travel times and calculated travel times are then inverted for seismic velocities everywhere in the model space using a linearized least-squares approach (Van Avendonk at al., 1998; Van Avendonk et al., 2001). This process of calculating raypaths in the new model and then producing a new velocity model with a least squares inversion is repeated until a minimum data misfit is achieved. In 9 iterations, the residual mean data fit reduced from 672 ms to 95 ms and the chi-squared reduced from 44.53 to 0.67.

The iterative nonlinear tomographic inversion converged on two solutions that both achieve a good data fit. These two solutions differ in the nature of the low-velocity zone beneath Mt. Dent, to which the raypaths appear to be sensitive. To account for this, we averaged 12 seismic velocity models from consecutive iterations of the inversion passed the 9th iteration that produced an acceptable data misfit. This average represents our final, preferred velocity model, with a residual mean data misfit of 95 ms and a chi-squared of 0.67. Fig. DR6 shows the final seismic tomographic image with picked and calculated travel times. The standard deviation of the final model (using the 12 inversion results) was calculated (Fig. DR7). A resolution test was also carried out in order to show how well the final velocity model resolves a body that is 10 km-wide by 5 km-high (Fig. DR8). Table S1 summarizes the errors for all 18 OBSs.

Gravity

The shipboard gravity data were corrected to the Free-air Anomaly (FAA) (Fig. DR10, middle panel). This FAA was then modeled for density in the center portion of Line 2 where seismic control is best. Starting with velocity contours from the velocity model, four layers were defined: a water layer, an upper crustal layer, a lower crustal layer, and an upper mantle layer. These layers were then assigned densities and then forward modeled to match the FAA (Fig. DR10, bottom panel). The water layer has a density of 1.03 g cm^{-3}, the upper crustal layer has a density of 2.55 g cm^{-3}, the lower crustal layer has a density of 2.65 g cm^{-3}, and the upper mantle layer has a density of 3.33

g cm^{-3}. This modelling shows that Mt. Dent has relatively lower densities than the surrounding lithosphere to the east and west.

Magnetics

The summit of Mt. Dent is ~14 km east of the center of the MCSC, ~2 my of spreading judging by the long-term ~7.5 mm/yr half-rate, based primarily on magnetic anomaly 3A, 5A and 6, all in off-axis crust >5 Ma-old (Leroy et al., 2000). The protracted evolution of the Mt. Dent OCC is indicated by the edge of the central magnetic anomaly along its eastern edge and an older positive magnetic anomaly along its western edge (Fig. DR10, top panel) (Hayman et al., 2011). The ultraslow spreading rate renders the exact ages of these anomalies unclear, but we take the older edge of the central anomaly to be ~0.71 Ma and the youngest age of the next oldest positive anomaly to be the edge of anomaly 2A, ~3.3 Ma (Leroy et al., 2000).

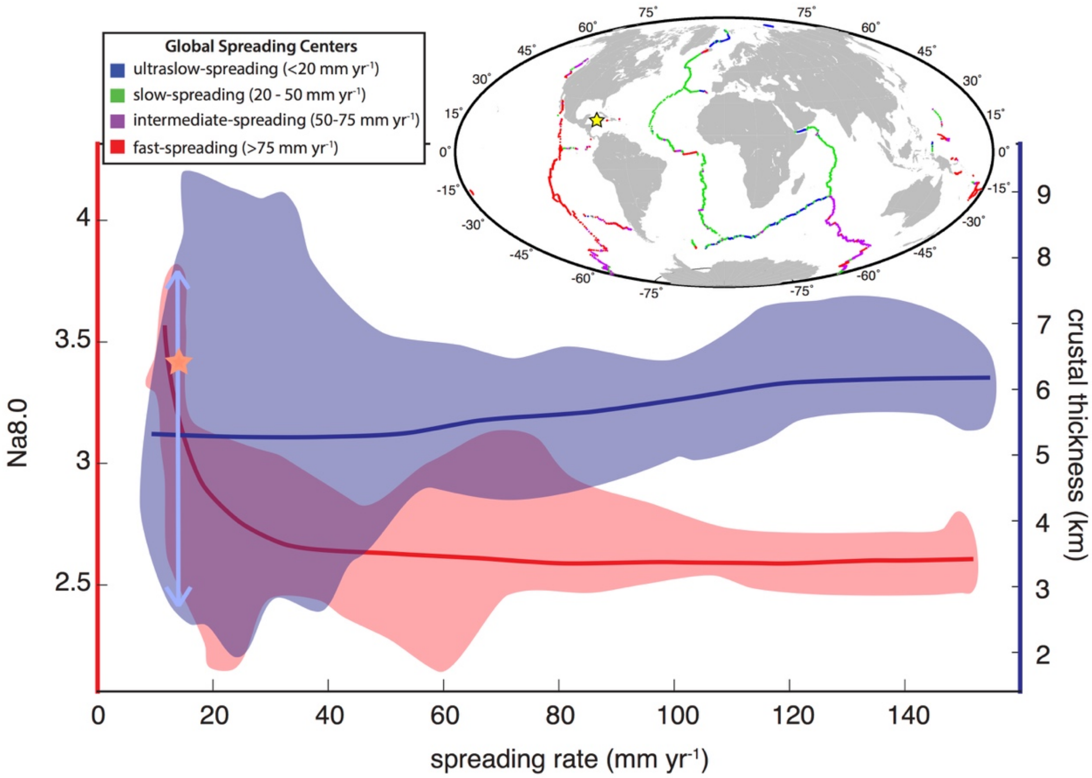

Fig. DR1:

Left-hand Y-axis is Na8.0 for segments of different spreading rate, incompatible element Na normalized to an MgO of 8.0 Wt. % in liquid-line-of descent models (Gale et al., 2014). Inset shows the location of the Mid-Cayman Spreading Center (MCSC) (yellow star) and several other ultraslow spreading systems in a global view. Crustal thickness values (right-hand Y-axis) are from a new compilation of seismic refraction studies conducted in the last 40 years. The plot illustrates that at spreading centers far from mantle plumes, incompatible elements become enriched and crustal thickness becomes more variable as a result of low extents of mantle melting when spreading rate drops to < 20 mm yr^{-1} (Dalton et al., 2014). The MCSC is important in this compilation because it has some of the highest Na8.0 concentrations (red star), and previously reported lowest

Publisher: GSA
Journal: GEOL: Geology
DOI:10.1130/G39045.1

crustal thickness values; as we show here the MCSC has highly variable crustal thickness over time (light blue line) (Fig. DR3).

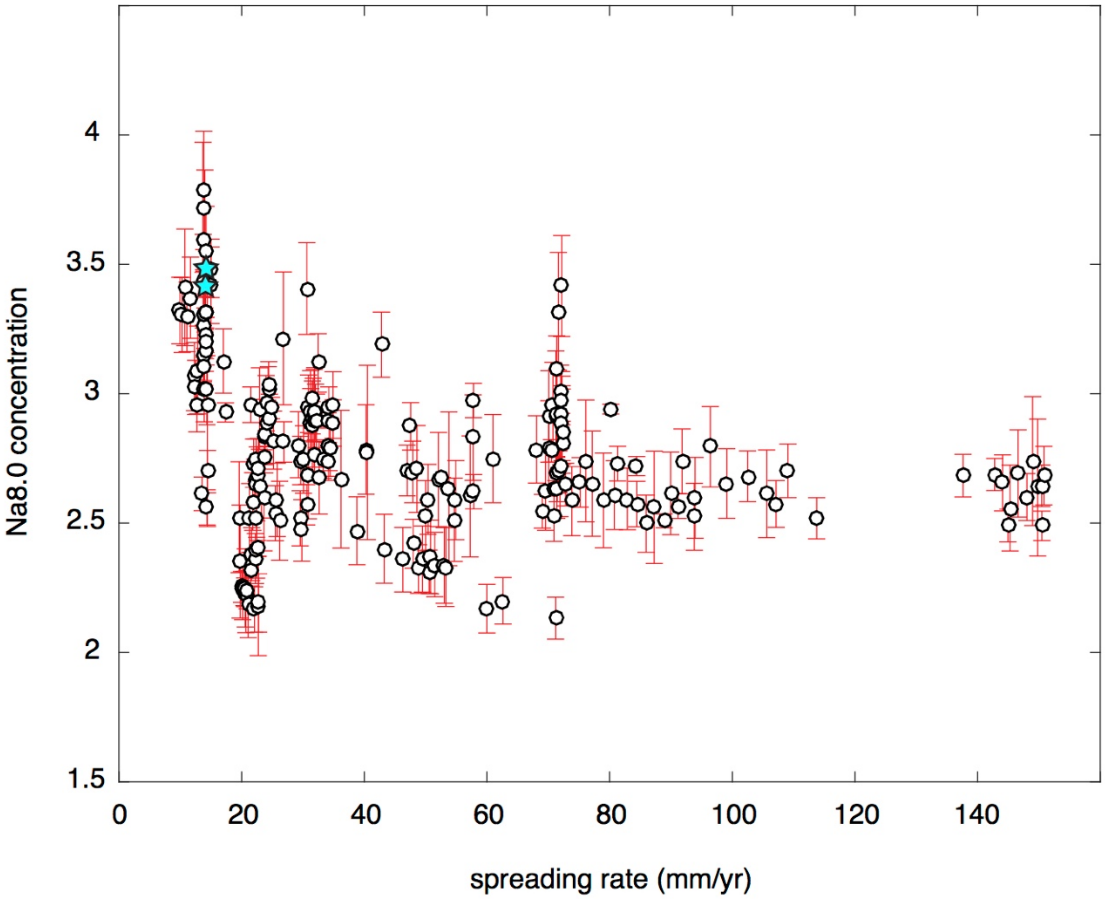

Fig. DR2

Na8.0 of basalts from segments of different spreading rates, where Na is normalized to an MgO of 8.0 Wt. % in liquid-line-of descent models (Gale et al., 2014). Data near hotspots were excluded from this plot. Mid-Cayman Spreading Center (MCSC) data is denoted by the cyan stars. At spreading rates slower than ~ 20 mm yr^{-1}, Na8.0 concentrations sharply increase, suggesting less mantle melting at ultraslow-spreading centers such as the MCSC.

Publisher: GSA
Journal: GEOL: Geology
DOI:10.1130/G39045.1

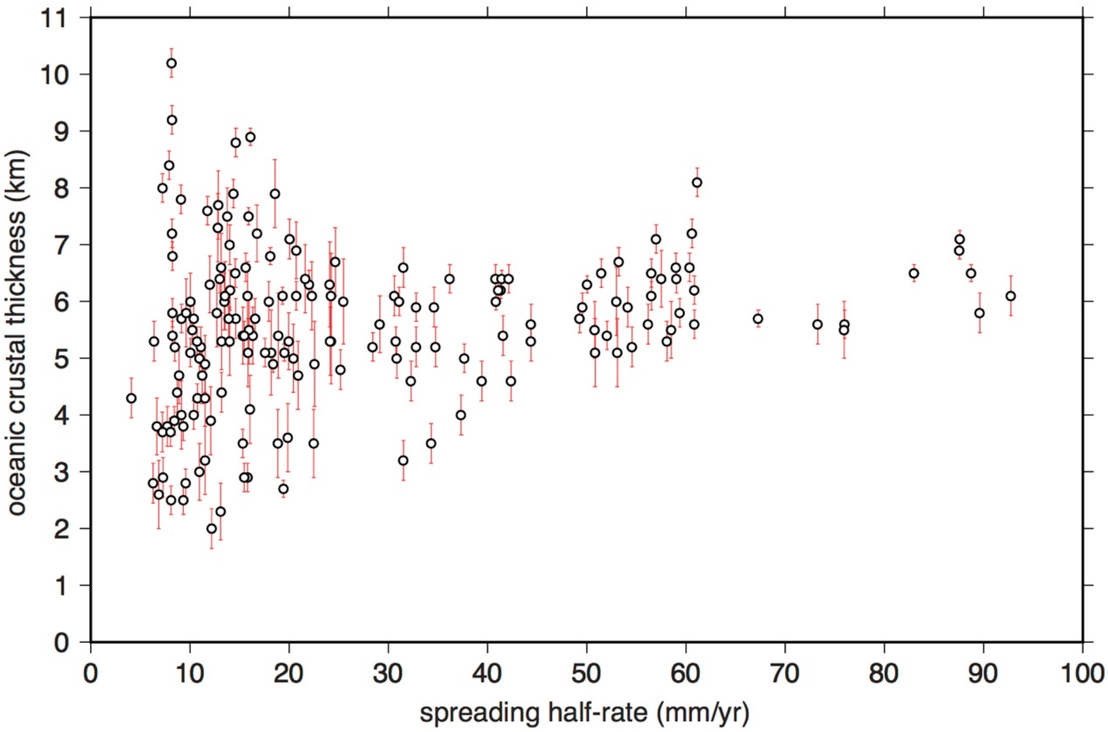

Fig. DR3

Oceanic crustal thickness vs. spreading half-rate from a compilation of seismically-determined oceanic crustal thicknesses. Crustal thickness estimates included are of oceanic crust younger than 20 Ma, collected since 1970, and away from hot spots or fracture zones. This database is included as a separate file (Database DR1). Oceanic crustal thickness averages ~ 6.0 km for spreading half-rates above 50 mm yr^{-1}, with crustal thickness decreasing slightly for slower spreading rates. A significant change in variability of crustal thickness can be observed at spreading half-rates lower than 50 mm yr^{-1}, showing that ultraslow-spreading centers like the Mid-Cayman Spreading Center behave differently from faster spreading centers.

DOI:10.1130/G39045.1

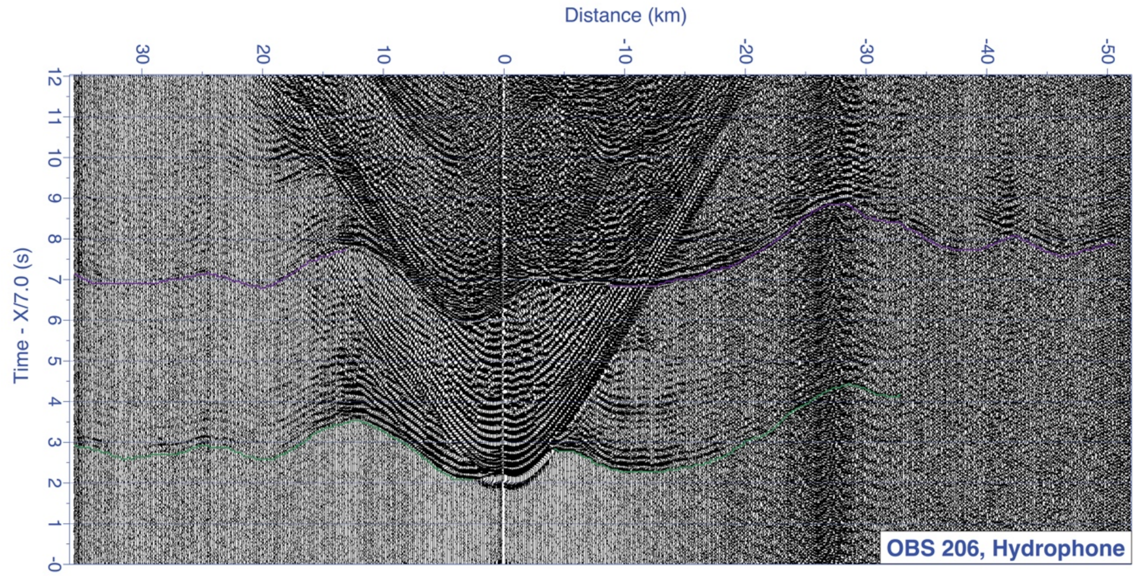

Fig. DR4

Wide-angle refraction data from the hydrophone channel of OBS 206, plotted as time at a reduction velocity of 7 km s^{-1}, and band-pass filtered between 5-15 Hz. The first-arrival P-wave travel-time picks are shown as green lines and the multiple P-wave picks are shown as purple lines.

Publisher: GSA
Journal: GEOL: Geology
DOI:10.1130/G39045.1

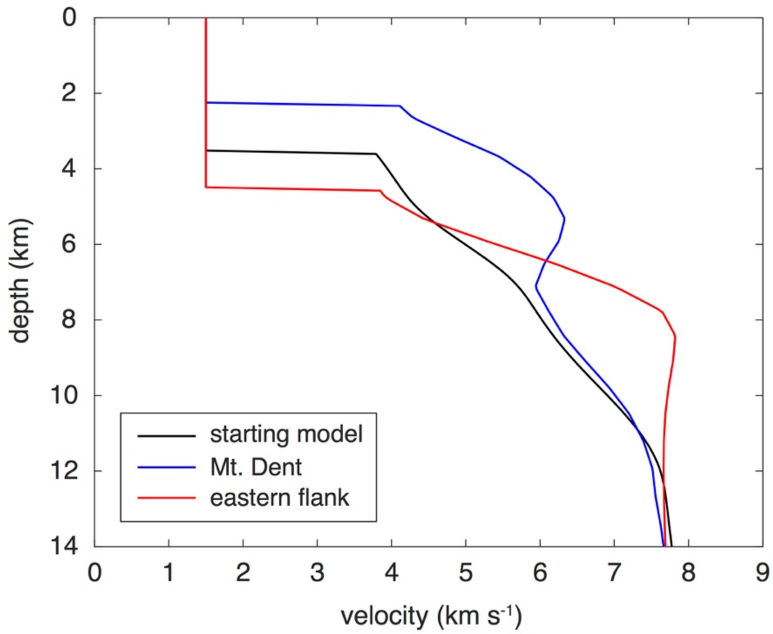

Fig. DR5

Velocity-depth profiles of the starting velocity model (black), Mt. Dent (red), and the eastern flank (blue), which correspond to the dotted lines in the bottom panel of Fig. S4.

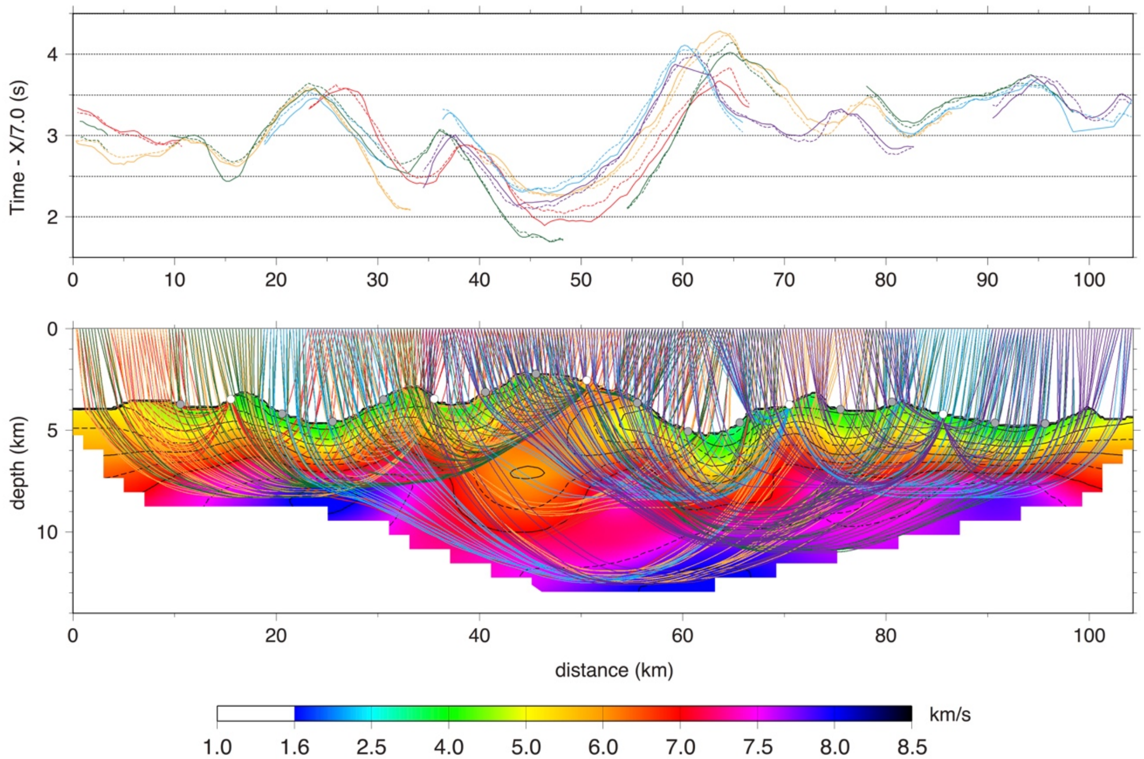

Fig. DR6

Raytracing diagram for the final seismic velocity model for Line 2. Top panel shows the picked (solid lines) and calculated (dashed lines) P-wave travel times, including multiples, plotted at a reduction velocity of 7 km s^{-1}, along Line 2. Colors indicate different OBSs that recorded these arrivals, which correspond to the bottom panel. The bottom panel shows the final seismic velocity model at 2x vertical exaggeration with raypaths for six different OBSs: 202 (red), 206 (orange), 209 (green), 213 (cyan), and 216 (purple).

DOI:10.1130/G39045.1

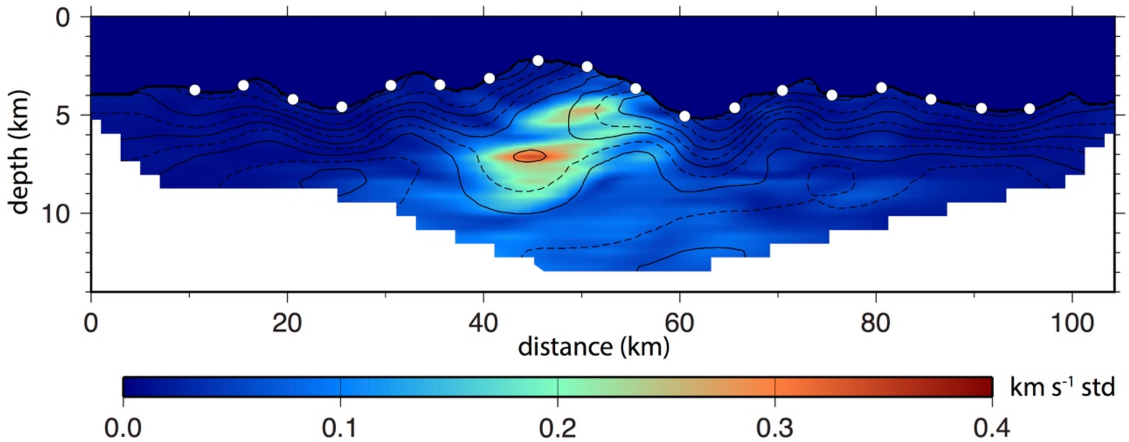

Fig. DR7

Standard deviation of the final seismic tomographic model at 2x vertical exaggeration. White circles are OBS locations. Standard deviations range from 0 to 0.4 km s$^{-1.}$ Most standard deviations are < 0.1 km s^{-1}, showing that the final model is stable; differences below Mt. Dent arise from the sensitivity of raypaths near the low velocity zone.

Publisher: GSA
Journal: GEOL: Geology
DOI:10.1130/G39045.1

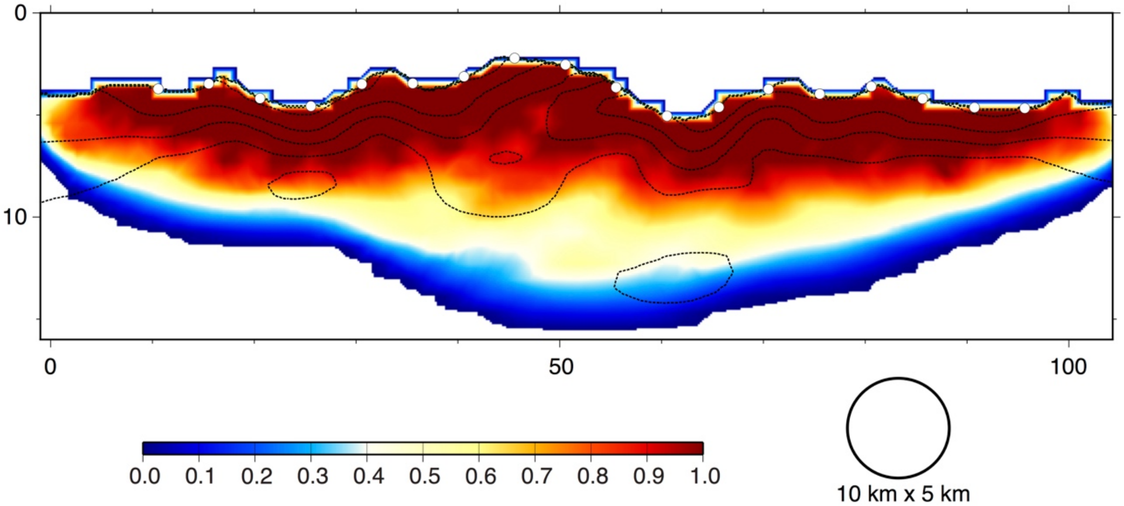

Fig. DR8

Line 2 resolution test for a 10 km-wide and 5 km-high body, plotted at 2x vertical exaggeration. A value of 1 (red) indicates full resolution of a body this size and a value of 0 (blue) means a body of this size cannot be resolved. OBSs are shown as white circles.

Table DR1:

OBS	Number of picks	Mean of travel-time residual (ms)	RMS misfit (ms)	Chi-squared
201	194	-24	78	0.583
202	168	-61	101	0.519
203	246	5	69	0.298
204	229	-5	58	0.424
205	183	-7	102	0.789
206	258	23	70	0.413
207	287	-69	88	0.735
208	218	-54	91	0.750
209	250	-8	88	0.628
210	143	145	198	3.017
211	295	7	58	0.370
212	255	101	151	0.831
213	202	-39	83	0.497
214	287	13	101	0.568
215	238	-37	74	0.583
216	201	8	79	0.959
217	185	29	89	0.472
218	73	76	108	0.586

Publisher: GSA
Journal: GEOL: Geology
DOI:10.1130/G39045.1

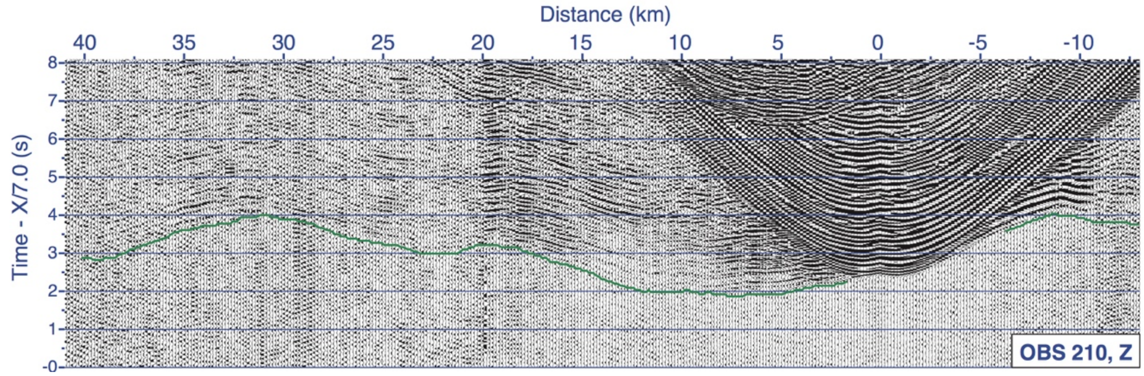

Fig. DR9

Wide-angle refraction data from the Z channel of OBS 210, plotted as time at a reduction velocity of 7 km s^{-1}, and band-pass filtered between 5-15 Hz. The first-arrival P-wave travel-time picks are shown as green lines and no multiple P-wave were picked for this instrument.

DOI:10.1130/G39045.1

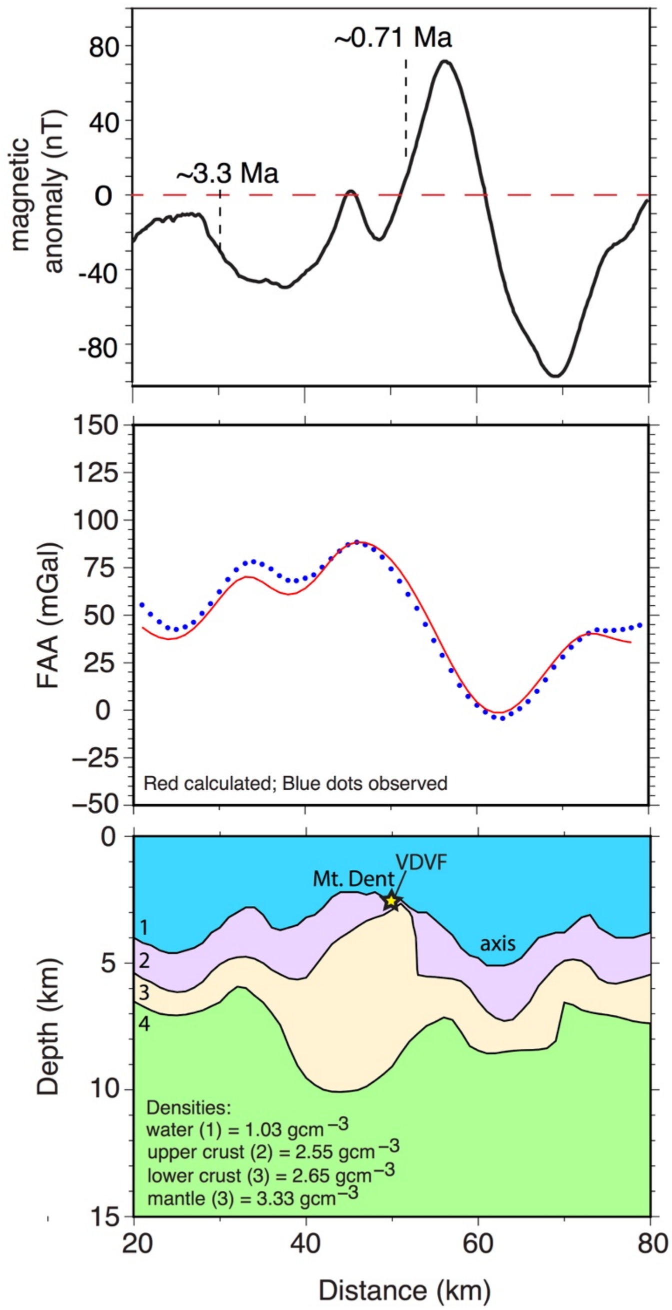

Fig. DR10

Top panel shows the shipboard gravity from Line 2, and the magnetic anomalies over the Mt. Dent detachment fault labeled with approximate reversal ages (Hayman et al., 2011). Middle panel shows the Free-air Anomaly (FAA) (blue dots) compared with the calculated FAA from density modelling (red line). Bottom panel shows the density model to produce the calculated FAA. The density model consists of (1) a water layer of density 1.03 g cm $^{-3}$, (2) an upper crustal layer of density 2.55 g cm^{-3}, (3) a lower crustal layer of density 2.65 g cm^{-3}, and (4) an upper mantle layer of density 3.33 g cm^{-3}. The gravity modelling shows that Mt. Dent has lower-crustal densities with a deep crustal root.

ADDITIONAL REFERENCES:

Leroy, S., Mauffret, A., Patriat, P., and Mercier de Lepinay, B., 2000, An alternative interpretation of the Cayman trough evolution from a reidentification of magnetic anomalies: Geophysical Journal International, v. 141, p. 539-557. doi:10.1046/j.1365-246x.2000.00059.x

Müller, R.D., Sdrolias, M., Gaina, C., and Roest, W.R., 2008, Age, spreading rates, and spreading asymmetry of the world's ocean crust: Geochemistry, Geophysics, Geosystems, v. 9, no.4, doi:10.1029/2007/gc001743.